Experimental Mechanics
https://doi.org/10.1007/s11340-020-00604-6

RESEARCH PAPER

Investigation of the Effect of Artificial Internal Defects on the Tensile Behavior of Laser Powder Bed Fusion 17–4 Stainless Steel Samples: Simultaneous Tensile Testing and X-Ray Computed Tomography

F.H. Kim [1] · S.P. Moylan [1] · T.Q. Phan [1] · E.J. Garboczi [2]

Received: 29 July 2019 / Accepted: 4 May 2020

Abstract

Insufficient data are available to fully understand the effects of metal additive manufacturing (AM) defects for widespread adoption of the emerging technology. Characterization of failure processes of complex internal geometries and defects in metal AM can significantly enhance this understanding. We aim to demonstrate a complete experimental measurement process and failure analysis method to study the effects of AM defects. We utilized simultaneous implementation of tensile tests with high-resolution X-ray computed tomography (XCT) measurements on 17–4 stainless steel dog-bone samples with an intentional octahedron-shaped internal cavity included in the gauge length and also containing much smaller lack-of-fusion (LOF) defects, all generated by a Laser Powder Bed Fusion (LPBF) additive manufacturing process. The LOF defects were introduced by intentionally changing the LPBF default processing parameters. XCT image-based linear elastic finite element (FE) simulations were used to interpret the data. The in-situ tensile tests combined with simultaneous XCT measurements revealed the details of the failure process initiated by additively manufactured rough internal surfaces and porous defect structures, which experienced high stress concentrations. Progressive collapse of ligaments leading to larger pores was clearly observed, and the resulting porosity evolution until failure was quantitatively analyzed. The high stress concentrations were also directly confirmed by the FE simulations. The experimental methods described in this paper enable the quantitative study of the complex failure mechanisms of additively manufactured metal parts, and the image-based FE simulation method is effective for identifying and/or confirming possible failure locations and features.

Keywords Artificial defects · Intentionally-seeded defects · Additive manufacturing · Effect of defects · In-situ mechanical test · X-ray computed tomography

Introduction

Additive Manufacturing (AM) is becoming an increasingly viable alternative manufacturing technique. While various materials (polymer, ceramic, and metal) are used for AM, metal AM has a greater potential to impact a wide range of industries including aerospace, biomedical, and automobile by producing load-bearing structural components with a more efficient functional design and reduced overall mass. Feedstock materials are generally in the form of powder, wire, or sheet, and energy sources such as lasers, electron beams, electric arcs, or ultrasound are currently utilized in different metal AM processes [1–3]. Although AM processes are still at a relatively early stage, the laser powder bed fusion (LPBF) AM process has already been used to produce parts for real-world applications such as fuel injection nozzles for airplane engines [4]. In order to qualify the part, however, many test samples had to be empirically tested. A different qualification framework to reduce the time and expense of such efforts can be realized by understanding fundamental failure mechanisms in these complex parts.

One of the major concerns of metal AM is the formation of defects that are different in size and characteristics from those of conventional manufacturing processes (e.g. casting). These defects are currently being categorized by international

✉ F. H. Kim
felix.kim@nist.gov

[1] Intelligent Systems Division, National Institute of Standards and Technology, Gaithersburg, MD, USA

[2] Applied Chemicals and Materials Division, National Institute of Standards and Technology, Boulder, CO, USA

Published online: 30 June 2020

standards organizations, but their effects are not yet well-understood. These defects include gas pores, lack-of-fusion (LOF) pores, keyholing pores, and cracks, which are all potential failure initiation sites [5–8]. Another concern of an AM-produced part is the inherently-rough surfaces, in the case of LBPF is on the scale of the median powder size, which can be critical for fracture and fatigue. These surfaces may be improved with post-manufacturing operations, but internal surfaces are often difficult to access for post-manufacturing operations. Furthermore, near-surface pores were found in several mechanical test samples produced with AM processes [9–11], which may be connected to the surfaces through micro cracks. AM-produced parts are not always perfectly built to the original computer-aided design (CAD), depending on the surface orientations (e.g. overhang or downward facing surface) [12], so as more custom and complex parts are designed and built using AM, the effect of this type of imperfect build quality also needs to be taken into account.

As medical and aerospace industries have great interest in using AM for their parts experiencing complex loading conditions [13], it is critical to detect defects prior to part installation. However, when a part is built containing complex external and internal geometry, almost all other non-destructive evaluation techniques fail to inspect the part, leaving X-ray Computed Tomography (XCT) the only viable option [14]. XCT provides a unique opportunity to inspect these types of parts non-destructively [15], and determining the probability of detection (POD) is a critical aspect of qualification [16]. AM is expected to be used in industries targeting a low volume production of highly customized parts, and individual inspection of custom parts may be needed to ensure the quality of the part. Coupon tests may not be representative of actual part geometry due to differences in thermal histories. Therefore, a direct test on the actual AM-produced parts may be needed, and a method to predict mechanical performance would significantly enhance the qualification process.

In addition to non-destructive inspection, XCT is also very useful for investigating the structure of various materials and any changes under applied loads (not just mechanical) [17], including geomaterials [18–23], composite materials [24–27], and metals [15, 28]. Advanced XCT systems can provide micrometer to sub-micrometer resolution with acquisition time of a few minutes to hours depending on applications (e.g., sample size, voxel size, X-ray power, source-to-detector distance, and number of projections required). Synchrotron imaging facilities provide similar resolution (≈ 1 μm or less) but at a much faster acquisition rate (≈ minutes or less per scan) due to significantly higher flux of the X-rays [29]. While most XCT experiments are ex-situ, in-situ experiments, with simultaneous loading and imaging, where one can monitor intermediate steps of the failure process, are being increasingly used at both synchrotron facilities and laboratory XCT systems [30, 31]. State-of-the-art synchrotron imaging beam lines are usually over-booked, and access to the facility is often limited. On the other hand, a laboratory system can be accessed more easily. An advanced laboratory XCT system provides similar resolution (≈ 1 μm or less) to that of a synchrotron facility, but it generally requires much longer acquisition time (minutes to hours), which does not allow a true dynamic study. In the case of a mechanical test, pseudo-static tests (interrupted tests) are generally conducted at different load increments. It is possible to perform dynamic XCT experiments at a synchrotron facility by rotating the sample at a high rate [32], but this requires a very small sample with low attenuation and a slower loading rate. The image quality may not be optimal for image thresholding and a quantitative analysis, as the exposure time is made as small as possible.

In this paper, in-situ mechanical tensile tests were carried out during XCT imaging to study the effects of defects and internal geometry with rough surfaces on the failure mechanism. We demonstrated the capability of in-situ mechanical tests and the ability to predict failure locations through image-based Finite Element (FE) simulations, focusing on uniaxial tensile loading. The effect of these defects in cyclic loading is also a critical problem [33], and it has recently been studied for AM materials [34, 35]. Interrupted in-situ mechanical tests were performed to directly visualize the material state under the applied load. Pore growth and crack formation were found. One of the strengths of XCT is the ability to resolve actual material structure and defect distribution, which provides an opportunity to directly perform FE simulation, with the actual voxels serving as the finite elements. We present a methodology to validate the FE simulation results with the experimental results of in-situ mechanical tests. This paper provides the entire workflow and associated results for the selected tests. The technique presented here is a powerful method to carry out a more systematic failure analysis by logically relating the actual defect geometry, location, and distribution to estimated stress concentrations and the failure process in the sample.

Materials and Methods

Sample Preparation

Cylindrical stainless-steel tensile samples were produced using a LPBF AM process with the EOS M270[1] system followed by a conventional machining process to refine and

[1] Certain commercial equipment, instruments, or materials are identified in this paper in order to specify the experimental procedure adequately. Such identification is not intended to imply recommendation or endorsement by the National Institute of Standards and Technology, nor is it intended to imply that the materials or equipment identified are necessarily the best available for the purpose.

polish the external shape. Surfaces produced with the LPBF process are generally rough enough so that they can dominate mechanical testing that was designed to interrogate internal defects, not external roughness. Two sample types were produced: One with a designed internal feature (Sample 1) and another with LOF pores generated by changing the LPBF processing parameters (Sample 2 and 3) from the vendor's default settings. The sample geometry is shown in Fig. 1(a), which was designed based on ASTM E8/E8M standards [36]. The samples were initially built 500 μm larger in radius to accommodate the final machining process. The tensile strength of the material and X-ray penetration were considered in determining the final size of the sample. A computer numerical control (CNC) machining process was applied to machine the samples to the desired final dimensions with smooth surfaces, along with grooves for the sample grips. An image of the final sample is shown in Fig. 1(b). Additional hand polishing with a fine-grit sand paper was performed on the gauge section. The samples were produced with the default LPBF processing parameters (Table 1) except for the regions of interest (ROIs) of Samples 2 and 3. Samples 2 and 3 incorporated LOF defects generated due to unoptimized LPBF processing parameters within the ROIs. The default processing parameters generally provide a nearly fully dense structure. Sample 1 has an internal designed feature, which is a hollow octahedron shape (Fig. 1(c)). Due to the LPBF process, powder particles are trapped inside the void. The angled surfaces were shown to be built closer to the original design, avoiding generation of dross on the top surfaces [12]. The ROI in Sample 2 was built with setting 1 (laser scan speed doubled from the default setting), and the ROI in sample 3 (hatch spacing doubled from the default setting) was built with setting 2 in Table 1. The theoretical energy densities associated with the different processing parameters were computed by using equation (1), and the energy densities of the two modified settings were identical as shown in Table 1. The energy density generally influences the part global density [3], but the actual pore structure may be different depending on the AM processing parameters as shown by XCT images [15]. Additional information on sample preparation may be found in a NIST internal report [37].

$$E = \frac{P}{v \cdot h \cdot t} \tag{1}$$

Pre-alloyed 17–4 stainless steel powders (GP1) [38] were used to produce samples with the chemical composition of typical 17–4 stainless steel. The powders were atomized in nitrogen gas, and the powder size, as measured by laser diffraction, was between 5 μm and 80 μm with a peak around 40 μm [39]. While wrought 17–4 stainless steel material is known to be fully martensitic, a GP1 powder-based 17–4 stainless steel component produced with the LPBF process was found to be composed of both austenitic and martensitic phases due to the retained nitrogen in the gas-atomized powders [40]. Phase transformation of the austenite to martensite was observed after a heat treatment or after applying some stress [41, 42]. For the samples in this experiment, a residual stress-relief heat treatment (650 °C for 1 h followed by quenching in nitrogen) was performed before removing the samples from the build plate [40]. The mechanical test results for the same materials and material characteristics are provided in other publications [40, 42].

Mechanical Testing

A load frame (Deben CT5000) designed for in-situ mechanical tests in XCT systems was used. The loading system mounts on the rotary stage of the XCT system as shown in Fig. 2(a), and the entire setup can rotate 360° for an XCT scan. The loading system is equipped with a 5 kN load cell for both tension and compression tests. A glassy carbon window allows high X-ray penetration while providing structural support. The sample is not optically visible through the glassy carbon window, and the operation of the mechanical loading must be monitored through X-ray imaging. The top of the sample is fixed to the top cover of the load frame, and the bottom of the sample is loaded toward the bottom of the load frame when loaded in tension as shown in Fig. 2(b). The sample is mounted between the grips as shown in Fig. 2(c). Copper wires were glued to the sample to help identify spatial locations within the XCT images.

XCT Acquisition

XCT is a non-destructive 3D imaging technique visualizing internal material structures. For a typical cone beam XCT scan, multiple radiographs (projections) of the object are acquired for a 360° rotation with a small angular increment. The acquired 2D projection images are combined using a reconstruction algorithm after completing the acquisition to produce a 3D reconstructed image volume representing attenuation values of the materials within this scanned volume. For this experiment, a ZEISS Versa XRM500 system was used as shown in Fig. 3. The loading system is mounted on the rotary stage. The desired geometric magnification was achieved by changing the ratio of the source-to-object distance and the source-to-detector distance, for a given lens. The detector is a lens-coupled charge coupled device (CCD) camera, which is a configuration typically used for synchrotron and neutron imaging [43, 44], unlike flat panel detectors of typical XCT systems. The X-rays produce visible light photons in the scintillation material coating the lenses, which then focus the light on the CCD camera. In addition to adjusting the geometric magnification, optical magnification can be adjusted by changing the lens with different magnifications. This feature

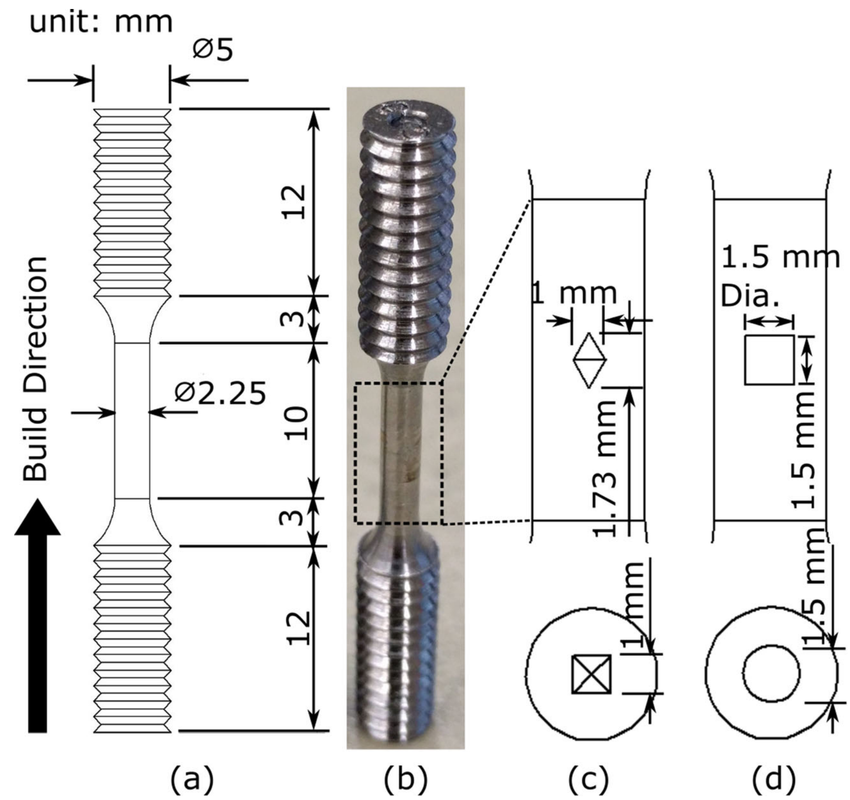

Fig. 1 External design of tensile test sample (**a**), picture of a tensile test sample (**b**), internal feature of sample 1 (**c**), and internal region (1.5 mm dia. × 1.5 mm height) where processing parameters are changed to generate LOF pores for samples 2 and 3 (**d**)

not only allows flexibility in achieving high spatial resolution, but also eliminates the need to place the sample too close to the X-ray source to achieve the highest resolution, which is important in case a bulky experimental setup needs to be installed on the rotary stage such as the load frame. A cable management system allows an easier manipulation of load frame cables during rotary stage movement. Two imaging settings were used: one at approximately 12 μm/voxel, and the other at about 3 μm/voxel. The voxel size and spatial resolution are related, but they are not identical. We denoted different XCT measurement settings in this paper using voxel size for simplicity, which should not be confused with spatial resolution. The spatial resolution of an imaging system is experimentally determined based on the Modulation Transfer Function (MTF) typically at 10% MTF [45, 46]. MTF is modeled as a Fourier transform of a system's comprehensive impulse response, which is a mathematical convolution of impulse responses of system components including geometric/optical magnification, effect of source spot size, scintillator light blooming effect, and detector pixel sampling rate [47, 48]. The spatial resolution is at least twice the voxel size, which is theoretically based on the Nyquist sampling theorem [49]. The maximum X-ray focal spot size is about 5 μm, and both geometric and optical magnification were adjusted such that geometric unsharpness did not exceed the effective pixel pitch of the detector. An XCT scan was acquired by measuring multiple projections of the sample by rotating the sample for a 360^o rotation with discrete angular steps. The number of projections were chosen to be more than the theory required [47], which is approximately $\pi/2$ times the number of pixels spanning the sample width. Details of the acquisition parameters are provided in Table 2. A filter was used to screen out lower voltage X-ray photons, so that at least 10% of the incident photons were transmitted through the sample.

XCT Reconstruction, Image Processing, and Segmentation

The acquired 2D projection images were reconstructed with a vendor-supplied cone beam filtered backprojection algorithm

Table 1 Processing parameter sets used for the AM builds

	Power, P (W)	Scan speed, v (mm/s)	Hatch spacing, h (mm)	Layer thickness, t (mm)	Energy density, E (10^9 J/m^3)
Default	195	1000	0.1	0.02	97.5
Setting 1	195	2000	0.1	0.02	48.75
Setting 2	195	1000	0.2	0.02	48.75

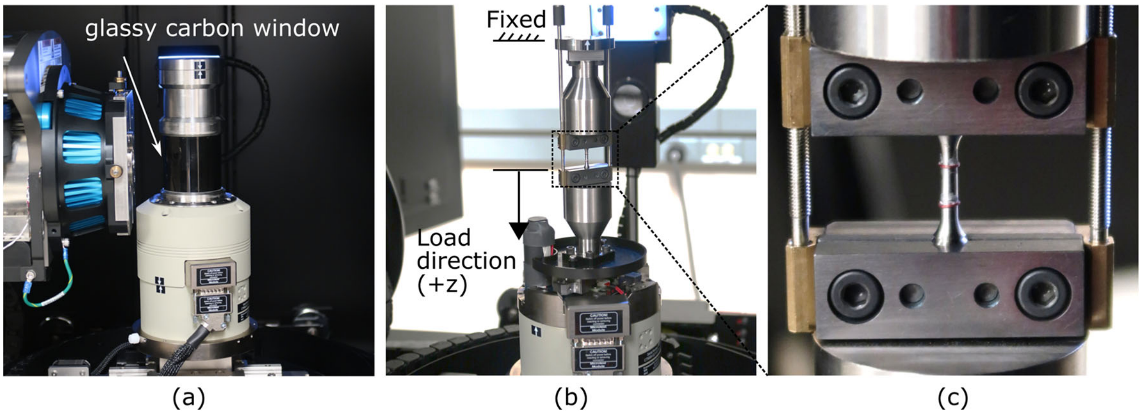

Fig. 2 (**a**) Load frame installed in the XCT system, (**b**) load frame with the cover off, and (**c**) a sample mounted in the load frame

[50], which is based on the Fourier slice theorem [51]. The algorithm is generally implemented by applying a filter on log-normalized projection signals in Fourier space, and the filtered signals are backprojected in the spatial domain to create reconstructed volume. The data were additionally corrected for beam hardening during the reconstruction process, which makes the image intensity more uniform. A non-local means filter was applied to the reconstructed images to reduce the noise level while minimizing blurring of the images [52]. VGStudioMax 3.1 was used to segment the data based on the advanced surface determination algorithm where applicable, and the VGEasyPore local thresholding algorithm was used to threshold pores in the samples for a quantitative analysis [53]. For smaller pores with lower grayscale contrast, the surface determination algorithm alone does not always successfully threshold the pores. Local thresholding algorithms such as Bernsen's method, which is very similar to the method implemented in VGStudioMax 3.1, significantly improves the possibility of detecting and thresholding pores [54]. A method, described in a recent paper [15], was used to find local contrast threshold values based on the noise level statistics of the images. An average of local standard deviation values within different homogenous locations of the volume was used as a basis to estimate an optimum local contrast threshold value larger than image noise level to avoid thresholding noise particles.

Interrupted Loading Experiments

Due to the relatively long acquisition time of an XCT scan compared to the strain rate of a typical mechanical test, discrete load increments were applied for the in-situ mechanical test. Aside from the applied rotation, it is crucial that the sample does not move during the XCT scan so as to avoid blurring the images. In this experiment, the sample was displaced at a constant crosshead speed (0.01 mm/min) until the load reached the target load, and then the load was held constant at this level. Due to the lack of programmable features in the control software, the crosshead movement stopped once it reached the load, and a manual command was implemented to hold the load at this level. During the initial stop of the crosshead movement, some load drop was experienced.

Fig. 3 XCT system setup with the in-situ loading system

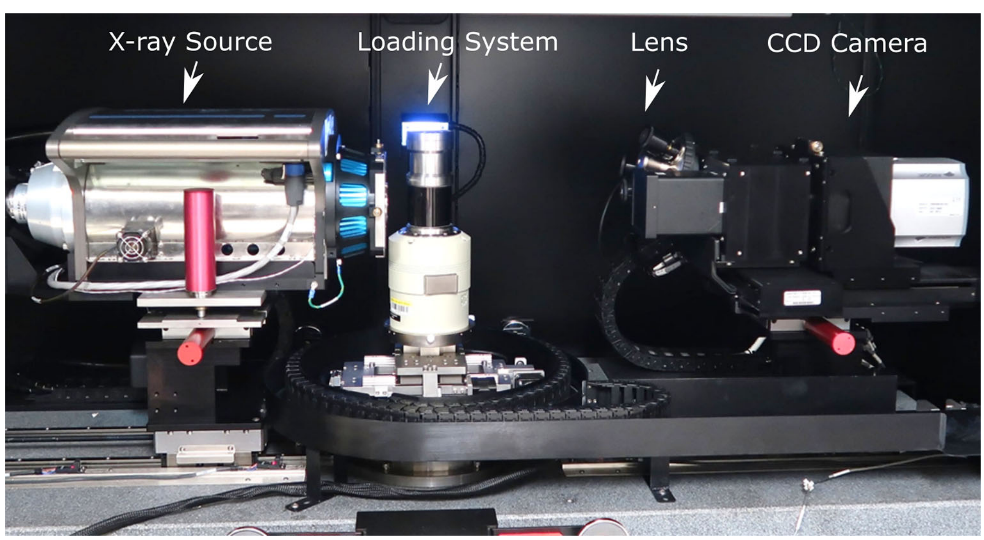

Table 2 XCT measurement settings

	Sample 1	Samples 2 and 3	
	Setting	Setting 1	Setting 2
Voltage (kV)	140	160	160
Power (W)	9	10	10
Geometric Magnification	5.68	5.62	2.23
Optical Magnification	0.4	0.4	4
CCD camera pixel (μm)	13.5	13.5	13.5
Binning	2	2	2
Exposure time (s)	4.2	5	23
Number of projections	300	300	1600
Effective Image Pixel (μm)	11.95	12.08	3.02

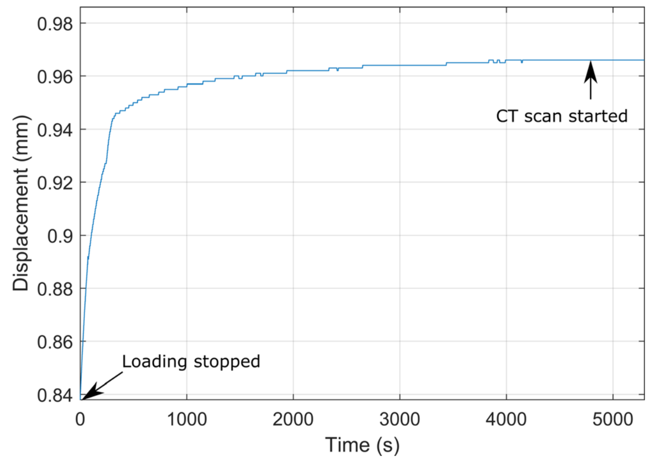

Fig. 4 Displacement curve vs. time showing equilibration of the displacement of sample 2 at load step 2

About 30 min to 1 h of equilibration time was required to stabilize any displacement change at a fixed load before starting an XCT scan. During this process, some displacement occurred in the sample. We described the phenomena creep in this paper as displacement occurred during a constant loading. Figure 4 shows the amount of creep, which is the displacement change occurring at a constant load until the displacement stabilizes over time. The rate of creep, which is the slope of the curve, decreased significantly over the stabilization time. After 1 h of stabilization time, any additional creep displacement was minimal, and the XCT scan was acquired. The amount of displacement change before and after the XCT scan was confirmed to be less than one voxel length, which did not affect the XCT scan results, as the reconstructed images were sharp in quality. An in-situ Synchrotron X-ray diffraction study confirmed the stress-induced phase transformation behavior of this material [55], and the creep was considered to be mainly due to this stress-induced austenite to martensite phase transformation as only a very small amount of creep was observed on a separate test performed on an equivalent wrought specimen geometry, not AM-built. Except for the section of glassy carbon window, all other parts of the of the load frame is made of 316 Stainless steel as the material. Based on the reported stiffness and strength of glassy carbon [56], compliance of less than 10 μm is estimated for 5 kN tensile loading. A complete understanding of this creep behavior would require a new study, since the origin of the creep was not the objective of the current study.

Finite Element Simulation

FE simulations were performed on the segmented 3D digital images using a custom-developed linear elastic simulation (FEM) code [57, 58]. In this code, each voxel is a tri-linear finite element and periodic boundary conditions are applied. The code is also parallel, so that hundreds of processors can be used to handle the hundreds of millions of finite elements used for a typical image stack. The FEM code captures all elastic displacement aspects inside and across voxels, and a complete solution is obtained, under linear elasticity, for any loading situation, with respect to the voxel size/feature size ratio. The 3D digital images that were created by stacking segmented image slices showed the cylindrical sample surrounded by air, so that the periodic boundary conditions were really only applied in the z-direction. Since there was no constraint on the x and y directions, a tensile strain applied in the z-direction determined the effective Young's modulus of each sample, similar to the experimental loading arrangement. The code applies a displacement in the loading direction, and outputs the stresses and strains averaged over each voxel.

The stress tensor elements in each solid voxel were combined into the von Mises stress, hydrostatic stress, and stress triaxiality factor quantities and stored in a file for the solid voxels. The triaxiality factor is the ratio of hydrostatic stress to von Mises stress [59]. The linear elastic simulation result does not track how the material voxels would fail, but high stress concentrations show areas where failure is likely to occur. The accuracy of the FE simulation depends on the ability to resolve and threshold small features and defects. While features below spatial resolution may not have been resolved, this is considered acceptable as larger defects are generally more critical to failure.

The FEM computation was run on the images from various strain steps, considering each image set to be under zero strain and stress before computational loading. The reason for this is the following. If image 2 was strained further from an already strained image 1, for example, then one cannot simply start with the strain field determined for image 1, add to the overall applied strain the extra applied strain between image 1 and image 2, and then determine the new strain field for image 2, since the voxels will not be precisely the same between the two image sets, due to the extra applied strain. On the other hand, one does not want to start with the zero-strain sample

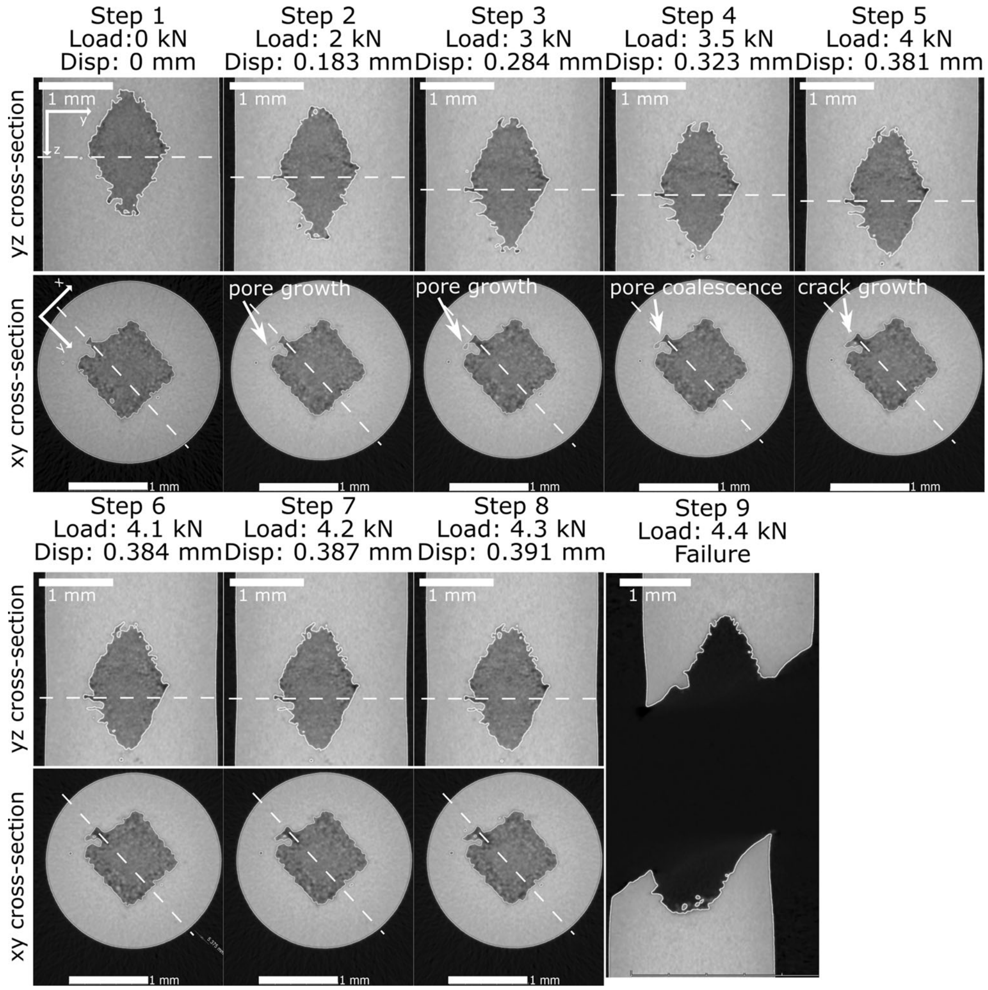

Fig. 5 Progression of failure of sample 1 through the loading steps

and keep on straining it linearly, since the FEM is only linear elastic and any actual pore changes, etc. at local high-stress sites are probably a non-linear effect. That is why a strain-free assumption was made for each image set, so that we could incorporate any non-linear effects on the pore structure from the actual experiment. This seemed like the best approach to incorporating the non-linear aspects of high-stress points while still using a linear elastic code.

Results and Discussion

Failure of an Internal Feature

Based on an ordinary tensile test of a similar specimen, seven different load steps were chosen and applied for testing Sample 1: 0 N, 2000 N, 3000 N, 3500 N, 4000 N, 4100 N, 4200 N, 4300 N, and 4400 N (failure). A loading rate of

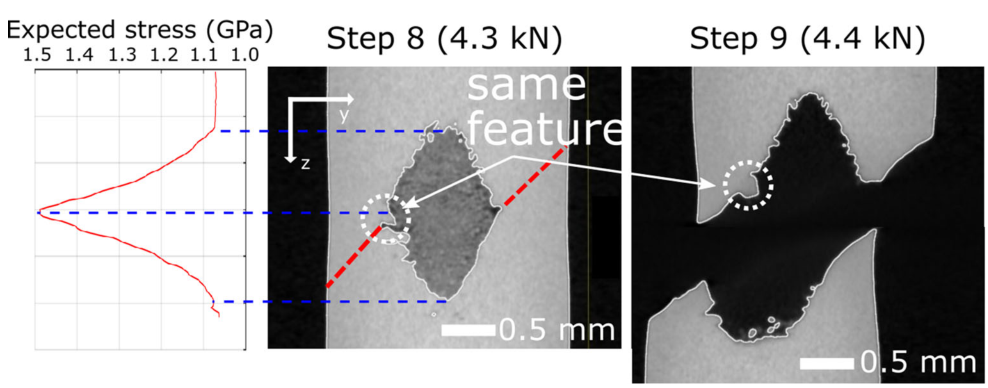

Fig. 6 Expected stress profile at step 8 in comparison to fractured surface of step 9 revealing fracture initiating features

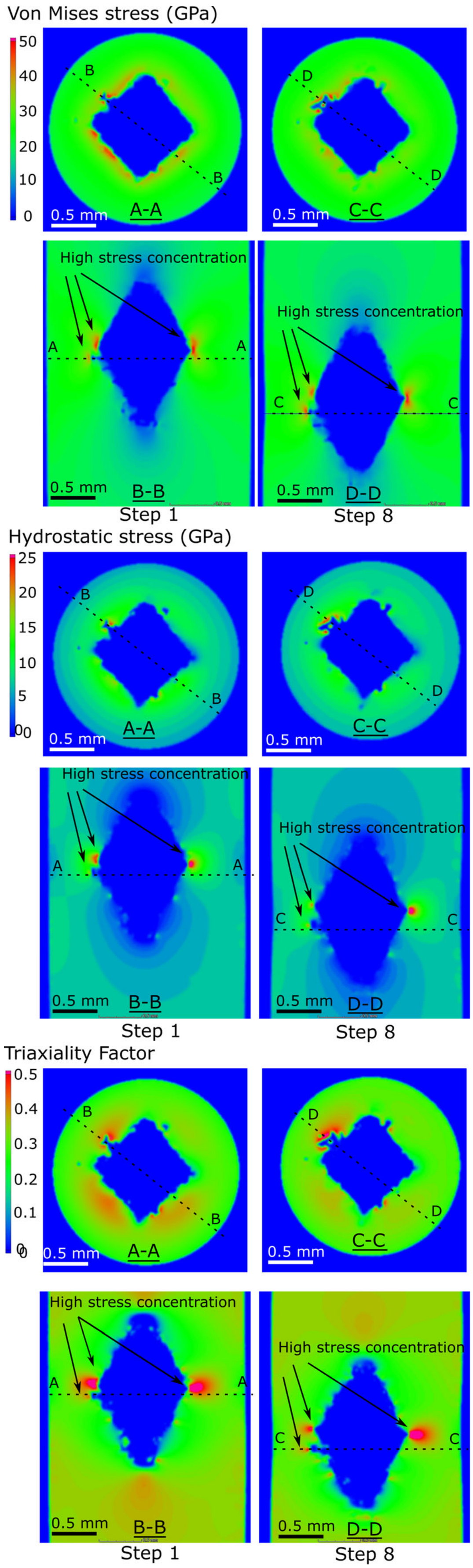

Fig. 7 FE simulation results of step 1 and step 8 of sample 1 showing high stress concentrations. A-A and C-C are the horizontal cross-sectional images of vertical cross-sectional images B-B and D-D, respectively

0.01 mm/min was used, and the sample was held at these load levels during the XCT scans. Since the voxel size of the XCT image was 12 μm, we expect the spatial resolution to be approximately 25 μm. For this reason, small gas pores are not likely to be resolved in this setting. Larger LOF pores and the designed internal cavity are more likely to affect the tensile failure due to their size and morphology. The progression of the mechanical test is shown in Fig. 5. The sample is pulled toward the bottom while the top of the sample is fixed, and the vertical (yz) and horizontal (xy) cross-sectional images are tracked at approximately the same locations. The XCT images of the original condition (step 1) shows the rough surfaces of the octahedral internal feature, which has some deviations from the designed shape. Such internal features cannot be improved with post-machining, and it is important to understand the effect of these imperfect rough surfaces on mechanical behavior. In step 2, a pore was observed close to the internal feature ahead of the crack tip in the horizontal (xy) cross-sectional image. This pore was not visible in step 1 prior to loading, and it is possible that this pore was smaller than the resolution limit prior to loading. As the load was applied, this pore grew in size and merged with the crack initiated from the internal rough surface, which is a typical ductile crack growth process. In step 4, the pore clearly coalesced with the internal feature. Due to the LPBF process, the interior of the large octahedron internal feature is filled with unmelted powder particles, which may be slightly sintered. As the internal feature deforms and cracks grow around the internal feature, the contrast around the boundary is improved. A darker region (example areas shown in step 8 of Fig. 5), which represents gas, is visible next to the internal surface instead of the unmelted solid powders. The darker region indicates additional crack growth and deformation of the internal feature. In step 4, the region of crack growth became even larger. Smaller load increments were applied until the final fracture with an attempt to capture the onset of failure and possible crack growth. Instead of a gradual crack propagation, the failure suddenly occurred at step 9. The sample broke at an angle of approximately 45°, indicating high shear stress.

Over the height of the sample at step 8, the cross-sectional area of the solid part was measured from XCT images in Fig. 6. The applied load (4.3 kN) at step 8 was divided by the cross-sectional areas to estimate the expected stress profile across two points along the height of the sample at step 8 as shown in Fig. 6. Due to the general geometry of the internal feature, we have the smallest cross-sectional solid area at the center of the internal feature, which is expected to have the highest stress and therefore fail at the center plane. When compared to the actual failed surfaces (step 9) from the XCT

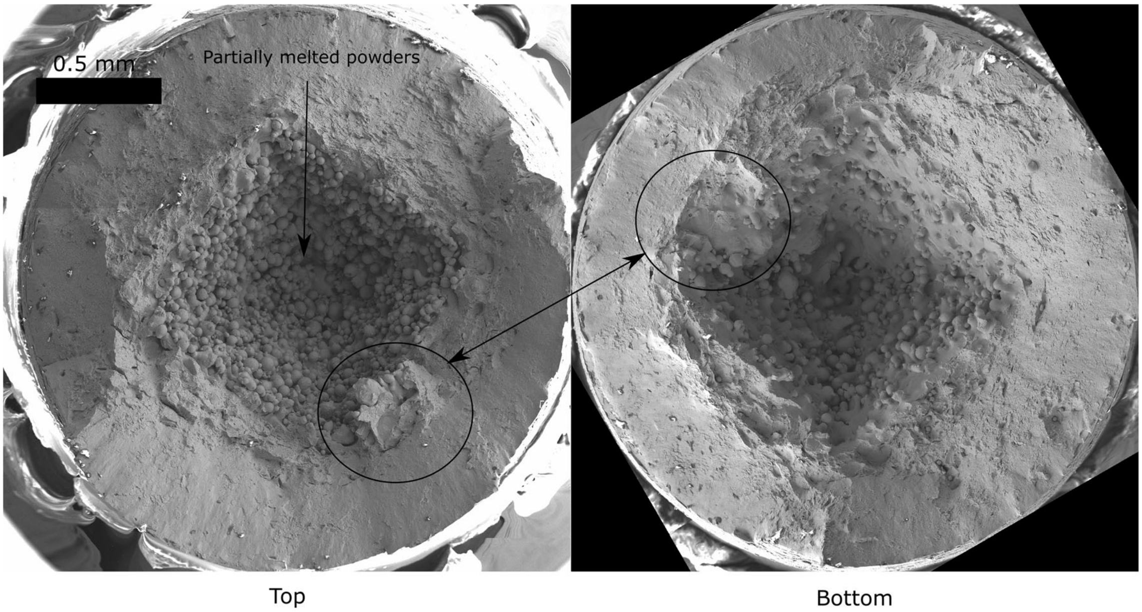

Fig. 8 Fractured surface SEM images of the top (LEFT image) and bottom (RIGHT image) of the octahedral defect. The highlighted features on the top and bottom surfaces are the same feature highlighted in step 9 of Fig. 6

images in Fig. 6, the sample failed at a little lower than the mid-height of the feature where a crack-like feature is present. A linear elastic FE simulation on the initial structure was performed, and von Mises stress, hydrostatic stress, and triaxiality factor are shown in Fig. 7 for every solid voxel – pore voxels have a von Mises and hydrostatic stress of zero, and triaxiality factor is undefined. A modulus of 200 GPa and a Poisson's ratio of 0.3 was used for each solid voxel, and a 10% linear strain was applied. As a linear elastic simulation was performed, the actual magnitude of the applied strain was not important, and we are only interested in the relative differences of stress experienced within the structure. A high correlation of failure-initiating locations from the experiment to the FE simulation was found as shown in Fig. 7, as follows. In the Step 1 part of Fig. 7, three high stress areas are shown in red. The same three high-stress areas are shown in the Step 8 part of Fig. 7, and one of these regions was the failure origin location. Therefore, even in Step 2 the FE correctly identified the true failure region as being a possible failure origin region. While there are some other locations experiencing similar stress concentrations, we believe the sample failed at the location identified in Fig. 6 as it has smaller root notch radius,

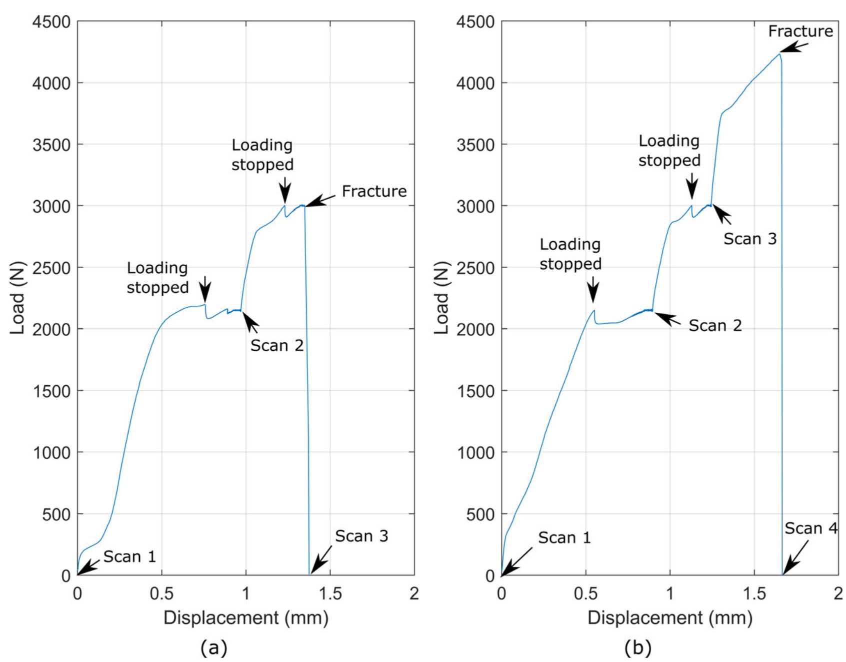

Fig. 9 Load-displacement curves of sample 2 (**a**) and sample 3 (**b**)

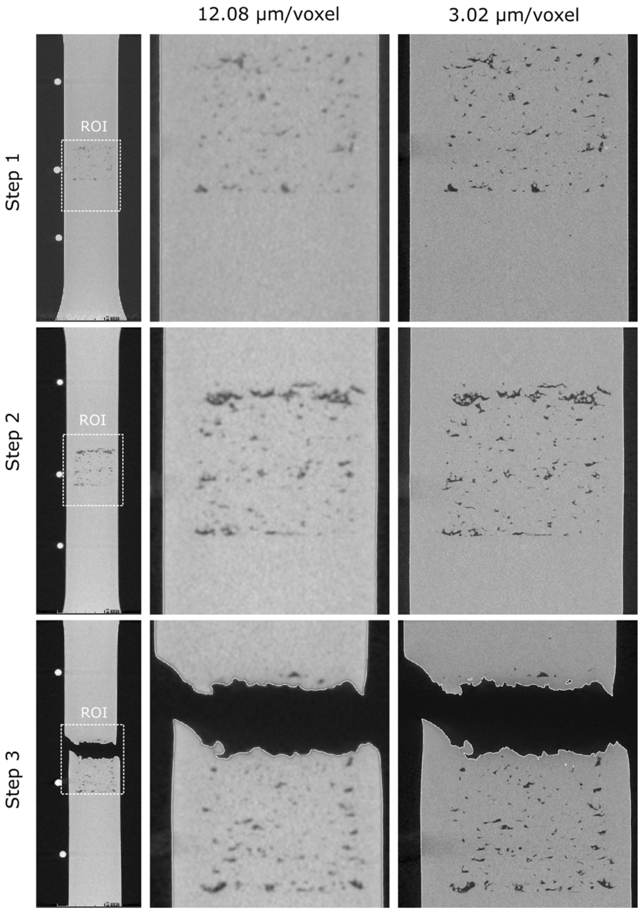

Fig. 10 XCT images at load steps of sample 2 and comparison of resolution

and higher stress was expected as the crack grew. Stress triaxiality is related to void growth inside the material, which was observed during the failure process [60, 61]. The local triaxiality factor image at step 8 shows a pore that grew in the region of high stress triaxiality. The trapped powders are not considered in the FE simulation, since they were taken out of the images via image analysis before the FE code was applied. These powders are lightly-sintered, and so they would contribute little to mechanical performance, even if included, especially in tension. SEM images of the fractured surfaces are shown in Fig. 8. The highlighted features on the top and bottom surfaces are the same features highlighted in step 9 of Fig. 6. The top surfaces of the octahedron internal feature have rougher surfaces compared to those of the bottom surfaces because they are downward facing. The unsintered trapped powders were removed after fracture.

Failure of Sample with LOF Pores

The samples with LOF defects (samples 2 and 3) were imaged at two different acquisition settings (12 μm/voxel and 3 μm/voxel). While the lower-resolution setting shows the entire gauge length, the higher-resolution setting focuses on the ROIs with defects. The samples have much smaller features/pore sizes compared to the relatively large internal feature of sample 1, and higher resolution was required to fully resolve the relevant features of interest. At each load step, the coarser resolution scan (scan time ≈ 30 min) was acquired first followed by the higher resolution scan (scan time ≈ 10 h). Acquisition of the coarser resolution scan before the higher resolution scan also provided the benefit of allowing additional time for sample stabilization prior to measuring with the higher resolution scan, which would be more sensitive to any drift in the sample displacement. The load displacement curves (Fig. 9) of the two samples both show an early yielding at around 2200 N, and a significant strain hardening toward

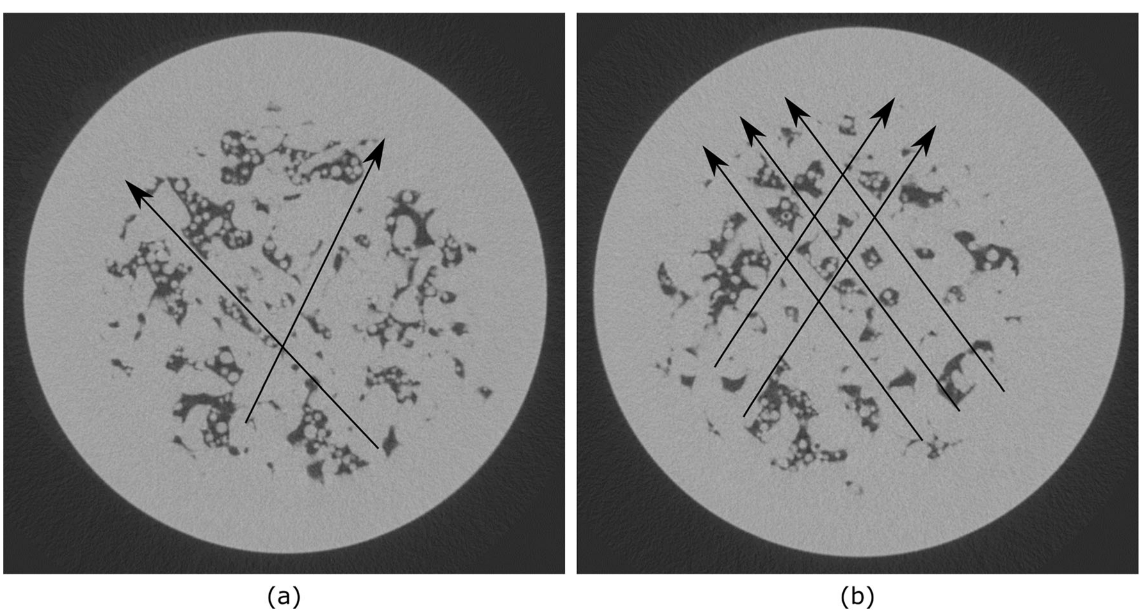

Fig. 11 Two-dimensional pore structure comparison of sample 2 (**a**) and sample 3 (**b**)

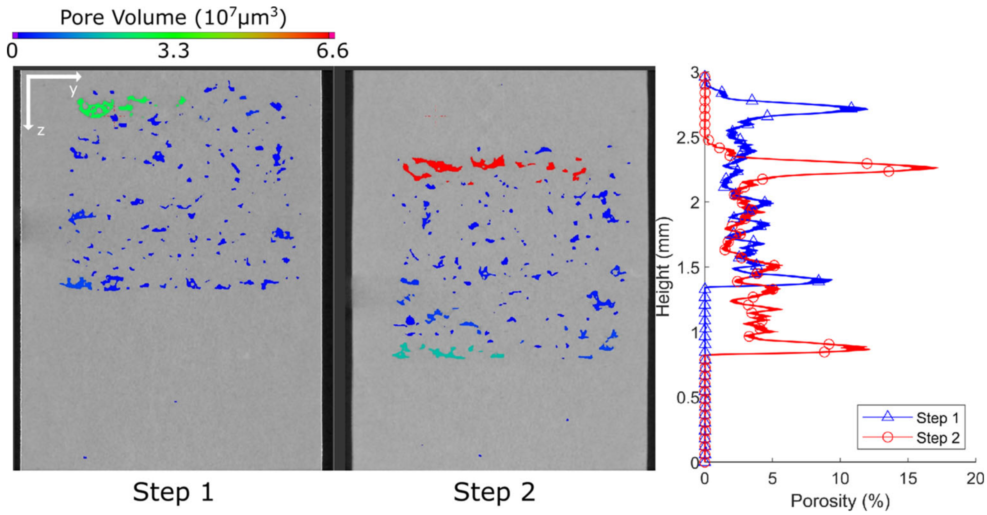

Fig. 12 Progression of 3-D pore size change and 2-D porosity over the height of sample 2

fracture, which corresponds to previous results on the same material [42]. While the sample was held at a constant load, a notable amount of displacement was observed in the load-displacement curve. This is thought to be due to the stress-induced phase transformation as explained earlier. Sample 2 failed at the 2nd load step, and Sample 3 failed at the 3rd load step.

The comparison of the two resolution settings at different load steps is shown in Fig. 10 for sample 2. The same procedure was also applied for the analysis of sample 3. Both the geometric magnification and optical magnification were adjusted to achieve the desired spatial resolution. The same ROIs were focused for comparison of resolution in Fig. 10. The higher-resolution images clearly resolve the defects with improved image contrast and will be used for the following quantitative analysis. Many times, it is not possible to know the ROIs prior to the experiment, and features are often hidden inside the sample. The coarser resolution setting may be used to quickly identify the ROIs of interest, and the higher resolution setting can be used to further investigate these chosen ROIs.

The pore structures of sample 2 and 3 are compared in Fig. 11. The locations of the reconstructed slices are at the top of the pore structure, near the region where failure ultimately occurred. The patterns are similar to previous results [15] presented for a CoCr alloy with the same LPBF system. The actual scanning parameters of 17–4 stainless steel are different from those of CoCr, but scan speed and hatch spacing were varied in a similar fashion. Example hatches are shown with arrows. The system rotates the hatch direction 67^{o}, and the angle between hatches with different direction is approximately 67^{o}. The individual hatches are more clearly shown in sample 3.

Connected networks of pores in samples 2 and 3 are labelled using different colors based on the size of their total volume in the thresholded images in Figs. 12 and 13, respectively. The thresholded porosity along the height of the ROI is also plotted for both samples 2 and 3, and high levels of

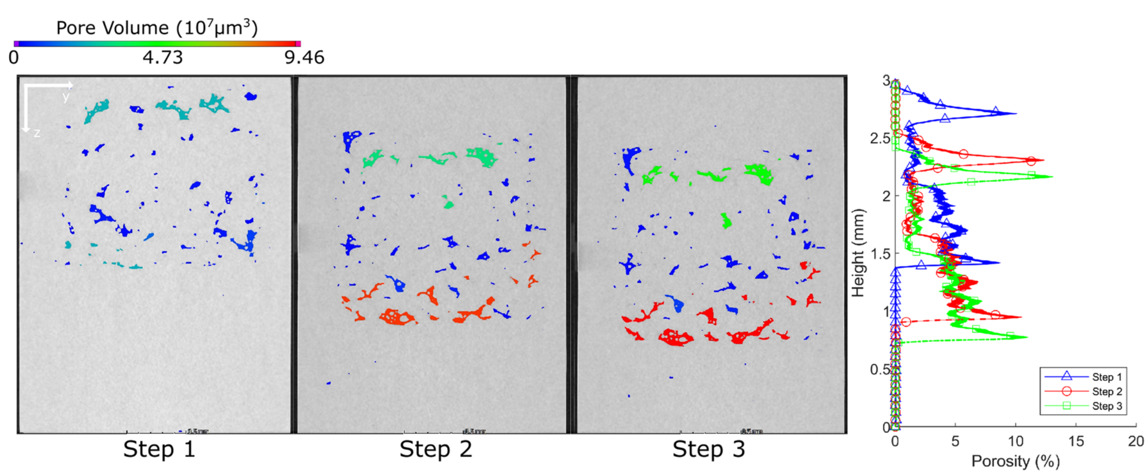

Fig. 13 Progression of 3-D pore size change and 2-D porosity over the height of sample 3

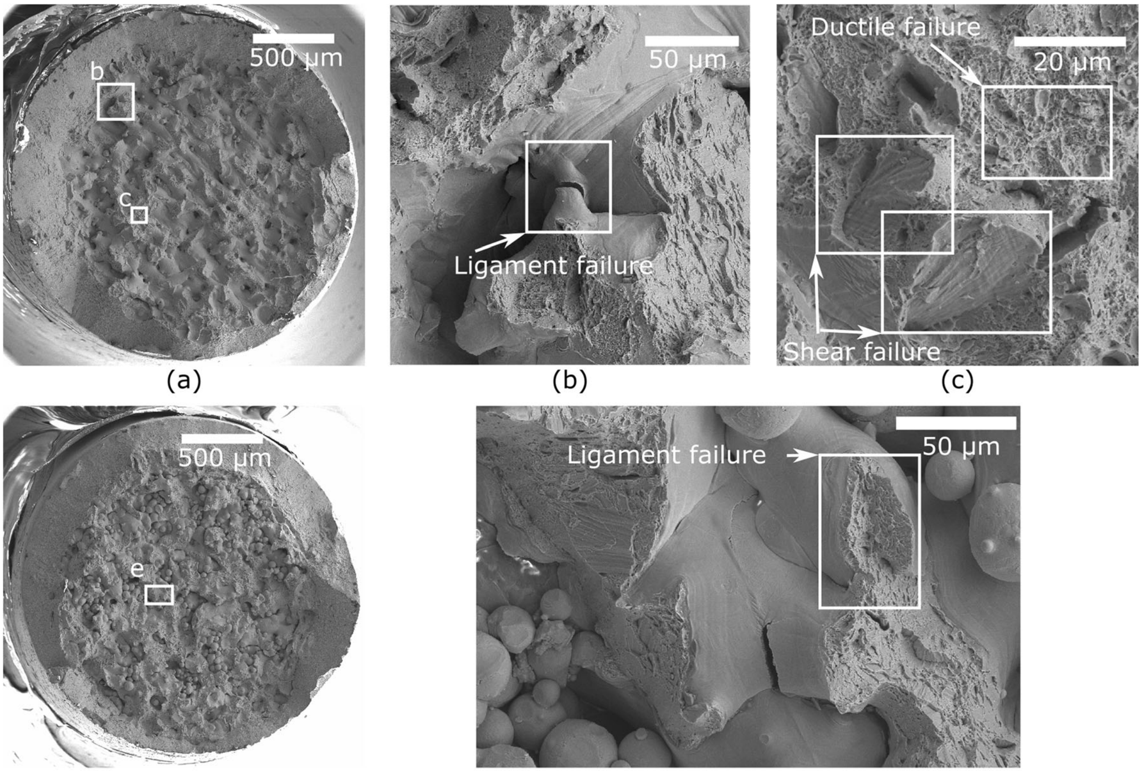

(a) (b) (c)

(d) (e)

Fig. 14 SEM images of (**a**) bottom fracture surface, (**b**) ROI showing a crack in a ligament (**c**) ROI showing shear failure, (**d**) top fracture surface, and (**e**) ROI showing a crack in a ligament of sample 2

porosity are observed at the top region of the LOF defect, which provides an explanation of the cause of failure at this location. The thickness of the line represents uncertainty envelopes of the porosity measurements due to the chosen local contrast threshold. The uncertainties were 1.19% for sample 1 step 1, 1.20% for sample 1 step 2, 1.00% for sample 2 step 1, 0.95% for sample 2 step 2, and 0.90% for sample 2 step 3. The largest connected pore is present at the top region of the LOF defect for sample 2, but at the bottom region for sample 3. The largest pore in the bottom of sample 3 has a larger volume because of smaller pores being connected vertically along the height, and so did not necessarily reduce the horizontal load-carrying area in the bottom of the ROI. The results may indicate a greater effect of the horizontal cross-sectional area for resisting vertical loads than the pore connectivity. At each load step, the 2-D porosity level increases, as shown from the computed porosity plot. The size of the connected pore increases, as indicated in the colorized pore volume shown for each set of XCT images. Progressive collapse of the original LOF defect ligaments that originally connected individual pores further reduced the cross-sectional areas for structural support. Failure of ligaments was observed clearly in the SEM images in Fig. 14(b), (e). The SEM images also reveal shear failure of some of the ligaments along with ductile failure in Fig. 14(c), for example. Other FE simulations were performed on the initial pore structure of the sample, and high stress concentrations were observed at some of the ligaments on the top interface for both sample 2 and 3 as shown in Figs. 15 and 16, respectively. The average von Mises stress, hydrostatic stress, and triaxiality factor were plotted over the height of the specimen, and they were calculated by dividing the sum of the quantity (von Mises stress, hydrostatic stress, or triaxiality factor) over each solid voxel in the cross section by the total number of such voxels. The average von Mises stress, hydrostatic stress, and triaxiality factor were found to have high values at the locations of failure for both samples.

An interesting aspect of sample 3 is that there happened to be a subsurface pore unintentionally produced close to the surface as shown in Fig. 17. The nature of formation of this pore is unclear, and it could be an end-of-track pore or LOF pore remaining after the post surface machining process. At step 1 prior to loading, the pore was clearly not connected to the surface. As the sample was loaded to step 2, the subsurface pore grew close to the surface. At step 3, the pore is finally connected to the surface. However, this surface connected crack did not initiate the failure for this particular sample and loading condition. While such subsurface or surface connected pores may be critical for failure in cyclic loading conditions, a static tensile test is probably more sensitive to the cross-sectional area of material resisting the load, plus internal defects.

Fig. 15 FE simulation results of sample 2 and average von Mises stress, hydrostatic stress, and triaxiality factor over height of the sample

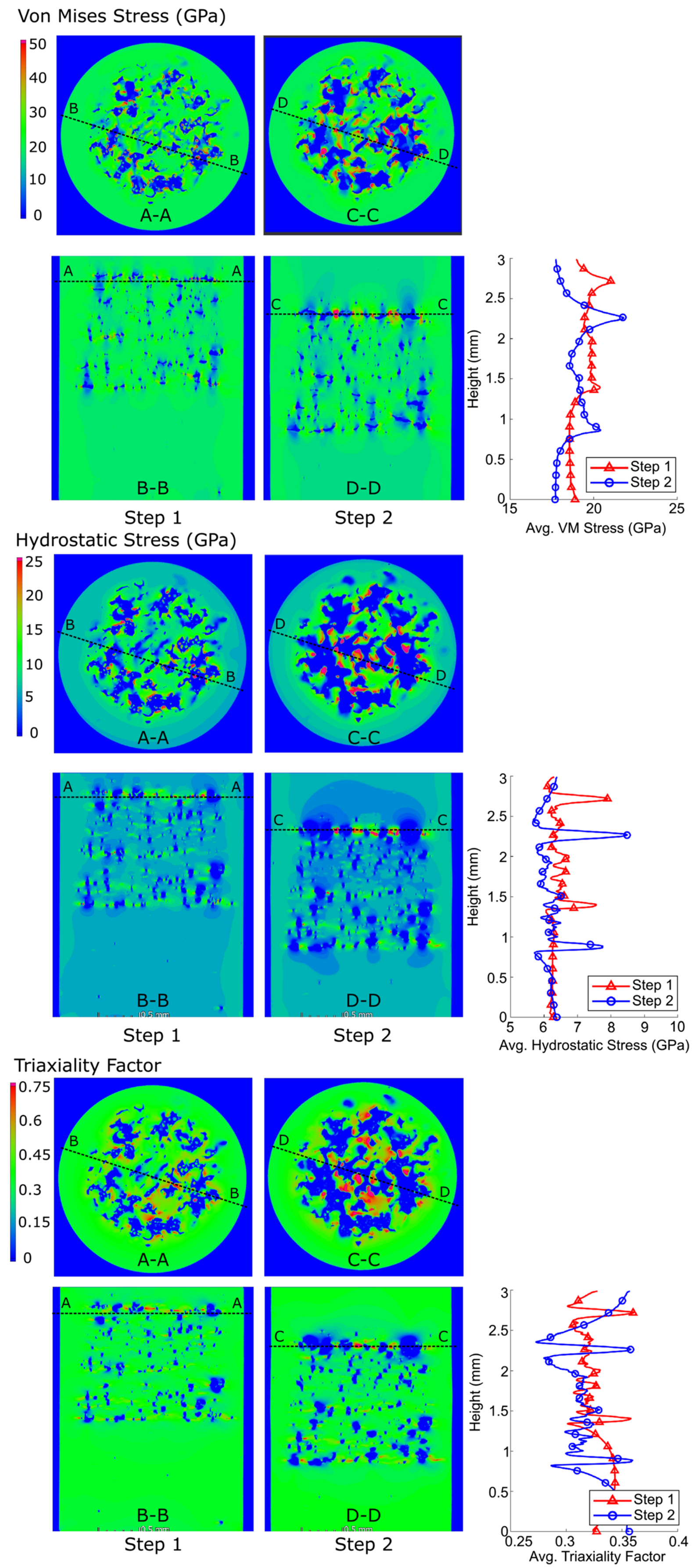

Fig. 16 FE simulation results of sample 3 average von Mises stress, hydrostatic stress, and triaxiality factor over height of the sample

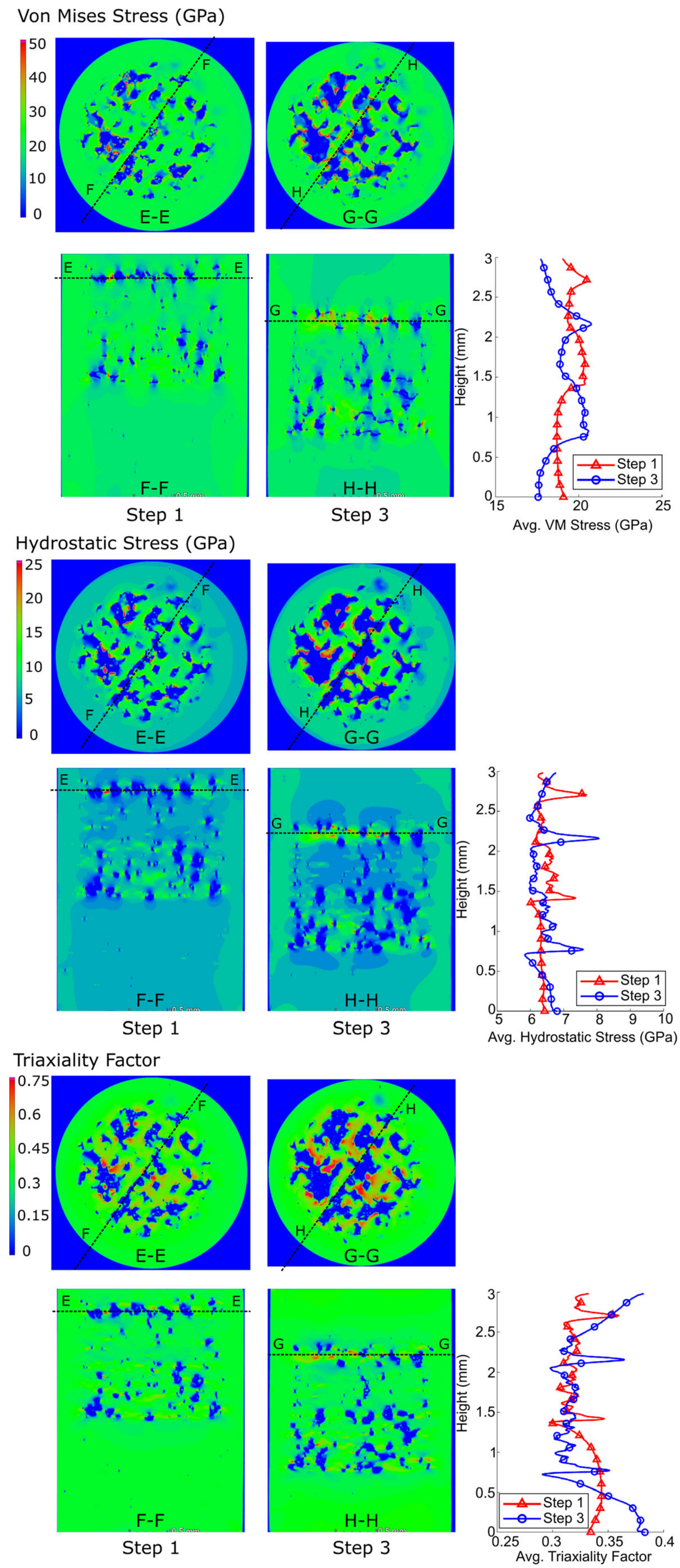

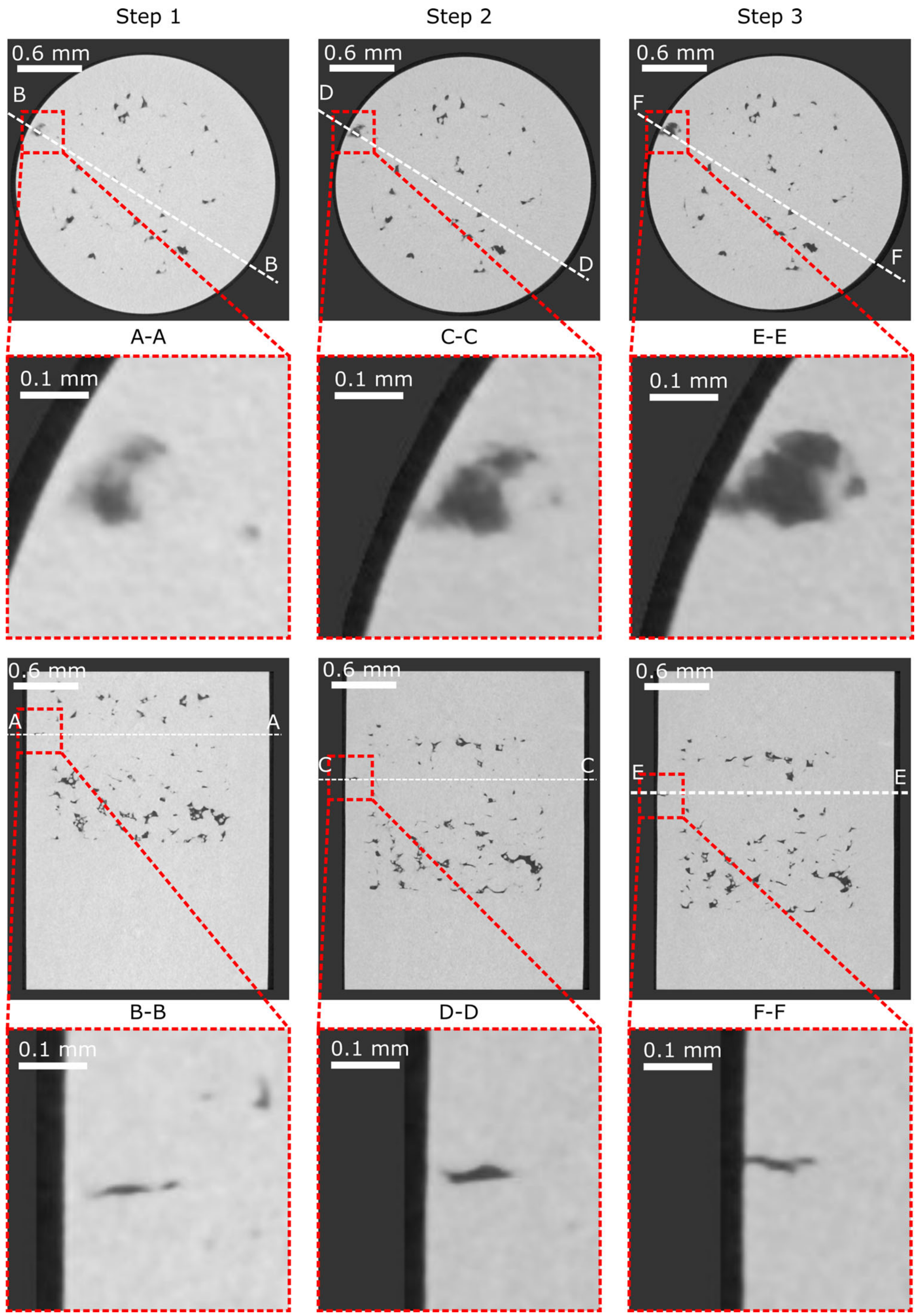

Fig. 17 Surface crack development originating from a subsurface defect in sample 3

Conclusions

We investigated the mechanical effects of a large AM-produced internal defect and LOF defects, produced by varying the optimal laser scan parameters, on the failure process by carrying out in-situ tensile tests during XCT measurements on AM 17–4 stainless steel samples. The internal LOF defects and designed features were embedded in the test samples through the LPBF AM process. The in-situ tensile tests revealed the 3D damage progression evolution, and FE analysis directly applied to the correctly-thresholded XCT images (elements = voxels) identified locations of high-stress concentration. While fracture of the sample with an octahedron-shaped internal feature initiated near the region with lower solid cross-sectional areas, the exact initiation location was slightly below the region, where a rough surface feature was present, causing high stress concentration. LOF defects generated at the center of the gauge length of the tensile samples failed at the top interface of the corresponding defect region. The quantitative analysis revealed higher 2-D porosity at this location, which also resulted in higher stress concentration when loaded. Struts separating disconnected pores progressively collapsed, which increased the overall porosity and pore sizes as the failure progresses. The process further increased stress concentration in the remaining struts resisting the failure until final fracture occurred. A sub-surface pore was observed in sample 3 that grew towards the surface as the load increased. This, however, was not the failure initiation point but could play a significant role in fatigue failure. The experimental methods described in this paper are promising methods to study complex failure mechanisms of additively manufactured parts, and the image-based FE simulation method is a promising predictive simulation tool to identify and/or confirm possible failure locations and features. AM allows greater manufacturing flexibility for developing unconventional complex structural designs. General understanding of the new material and effects of AM defects is still limited. It is important to understand the mechanical effects of AM defects and internal features, and the methods and results of the current study are expected to improve our overall understating of the subject.

Acknowledgements The authors would like to thank REX Heat Treat company for performing the heat treatment. We would also like to thank Dr. Jarred Heigel (Third Wave Systems), Mr. Mike McGlaughlin (NIST), and Mr. Jared Tarr (NIST) for assistance with the AM process and subsequent post-machining process. The authors would also like to thank Dr. Andrew Holmgren of Ball Aerospace, and Mr. Dash Weeks of NIST for assistance with preparation and carrying out the experiments. The authors would also like to thank Dr. Mark Stoudt and Dr. Lyle Levine of NIST for a useful discussion of the results. The authors thank Dr. Darren Pagan of the Cornell High Energy Synchrotron Source (CHESS) for fruitful discussion of the triaxiality factor.

Author's Contribution Contribution of the National Institute of Standards and Technology, not subject to copyright in the USA.

Compliance with Ethical Standards

Ethics Declarations This article does not contain any studies involving animals performed by any of the authors. This article does not contain any studies involving human participants performed by any of the authors.

Conflict of Interest The authors declare that they have no conflicts of interest.

References

1. Kruth JP, Leu MC, Nakagawa T (1998) Progress in additive manufacturing and rapid prototyping. CIRP Ann Manuf Technol 47:525–540. https://doi.org/10.1016/S0007-8506(07)63240-5
2. Murr LE et al (2012) Metal fabrication by additive manufacturing using laser and electron beam melting technologies. J Mater Sci Technol 28:1–14. https://doi.org/10.1016/S1005-0302(12)60016-4
3. Vandenbroucke B, Kruth JP (2007) Selective laser melting of biocompatible metals for rapid manufacturing of medical parts. Rapid Prototyp J 13:196–203. https://doi.org/10.1108/13552540710776142
4. McMasters MA, Benjamin MA, Mancini A, Lohmueller SJ (2014) Fuel Nozzle. USA Patent,
5. Ahsan MN, Bradley R, Pinkerton AJ (2011) Microcomputed tomography analysis of intralayer porosity generation in laser direct metal deposition and its causes. J Laser Appl 23:022009. https://doi.org/10.2351/1.3582311
6. Kim FH, Moylan SP (2018) Literature review of metal additive manufacturing defects. NIST Advanced Manufacturing Series (NIST AMS) 100-16. https://doi.org/10.6028/NIST.AMS.100-16
7. Kobryn PA, Moore EH, Semiatin SL (2000) The effect of laser power and traverse speed on microstructure, porosity, and build height in laser-deposited Ti-6Al-4V. Scr Mater 43:299–305. https://doi.org/10.1016/S1359-6462(00)00408-5
8. Ng GKL, Jarfors AEW, Bi G, Zheng HY (2009) Porosity formation and gas bubble retention in laser metal deposition. Appl Phys A 97:641–649. https://doi.org/10.1007/s00339-009-5266-3
9. Mancisidor AM, Garciandia F, Sebastian MS, Álvarez P, Díaz J, Unanue I (2016) Reduction of the Residual Porosity in Parts Manufactured by Selective Laser Melting Using Skywriting and High Focus Offset Strategies. Phys Procedia 83:864–873. https://doi.org/10.1016/j.phpro.2016.08.090
10. Thijs L, Kempen K, Kruth J-P, Van Humbeeck J (2013) Fine-structured aluminium products with controllable texture by selective laser melting of pre-alloyed AlSi10Mg powder. Acta Mater 61:1809–1819. https://doi.org/10.1016/j.actamat.2012.11.052
11. Yadollahi A, Shamsaei N (2017) Additive manufacturing of fatigue resistant materials: challenges and opportunities. Int J Fatigue 98:14–31. https://doi.org/10.1016/j.ijfatigue.2017.01.001
12. Kim FH, Villarraga-Gómez H, Moylan SP (2016c) Inspection of Embedded Internal Features in Additively Manufactured Metal Parts Using Metrological X-ray Computed Tomography. Paper presented at the ASPE/euspen 2016 summer topical meeting dimensional accuracy and surface finish in additive manufacturing, Raleigh, NC
13. Hrabe N, Barbosa N, Daniewicz S, Shamsaei N (2016) Findings from the NIST/ASTM workshop on mechanical behavior of additive manufacturing components. NIST Advanced Manufacturing Series (NIST AMS) 100–4. https://doi.org/10.6028/NIST.AMS.100-4
14. Todorov E, Spencer R, Gleeson S, Jamshidinia M, Kelly SM (2014) AMERICA MAKES: NATIONAL ADDITIVE MANUFACTURING INNOVATION INSTITUTE (NAMII) project 1: nondestructive evaluation (NDE) of complex metallic additive manufactured (AM) structures. AIR FORCE RESEARCH LABORATORY, WRIGHT-PATTERSON AIR FORCE BASE, OH 45433–7750
15. Kim FH, Moylan SP, Garboczi EJ, Slotwinski JA (2017) Investigation of pore structure in cobalt chrome additively manufactured parts using X-ray computed tomography and three-dimensional image analysis Addit Manuf 17:23–38 doi:https://doi.org/10.1016/j.addma.2017.06.011
16. Kim FH, Pintar AL, Moylan SP, Garboczi EJ (2019b) The influence of X-Ray computed tomography acquisition parameters on image quality and probability of detection of additive manufacturing defects. J Manuf Sci Eng 141. https://doi.org/10.1115/1.4044515
17. Buffiere J-Y, Maire E, Adrien J, Masse J-P, EJEM B (2010) In situ experiments with X ray tomography: an attractive tool for experimental mechanics. 50:289–305. https://doi.org/10.1007/s11340-010-9333-7
18. Alshibli K, Sture S, Costes N, Frank M, Lankton M, Batiste S, Swanson R (2000) Assessment of localized deformations in sand using X-ray computed tomography. Geotech Test J 23:274–299. https://doi.org/10.1520/GTJ11051J

19. Desrues J, Chambon R, Mokni M, Mazerolle F (1996) Void ratio evolution inside shear bands in triaxial sand specimens studied by computed tomography. Géotechnique 46:529–546. https://doi.org/10.1680/geot.1996.46.3.529
20. Kim FH, Penumadu D, Gregor J, Kardjilov N, Manke I (2013) High-resolution neutron and X-ray imaging of granular materials. J Geotech Geoenviron 139:715–723. https://doi.org/10.1061/(ASCE)GT.1943-5606.0000809
21. Kim FH, Penumadu D, Gregor J, Marsh M, Kardjilov N, Manke I (2015) Characterizing partially saturated compacted-sand specimen using 3D image registration of high-resolution neutron and X-ray tomography. J Comput Civ Eng 29:04014096. https://doi.org/10.1061/(ASCE)CP.1943-5487.0000424
22. Kim FH, Penumadu D, Kardjilov N, Manke I (2016a) High-resolution X-ray and neutron computed tomography of partially saturated granular materials subjected to projectile penetration. Int J Impact Eng 89:72–82. https://doi.org/10.1016/j.ijimpeng.2015.11.008
23. Turner AK, Kim FH, Penumadu D, Herbold EB (2016) Meso-scale framework for modeling granular material using computed tomography. Comput Geotech 76:140–146. https://doi.org/10.1016/j.compgeo.2016.02.019
24. Babout L, Maire E, Buffière JY, Fougères R (2001) Characterization by X-ray computed tomography of decohesion, porosity growth and coalescence in model metal matrix composites. Acta Mater 49:2055–2063. https://doi.org/10.1016/S1359-6454(01)00104-5
25. Brault R, Germaneau A, Dupré JC, Doumalin P, Mistou S, MJEM F (2013) In-situ analysis of laminated composite materials by X-ray micro-computed tomography and digital volume correlation. 53: 1143–1151. https://doi.org/10.1007/s11340-013-9730-9
26. Moffat AJ, Wright P, Buffière JY, Sinclair I, Spearing SM (2008) Micromechanisms of damage in 0° splits in a [90/0]s composite material using synchrotron radiation computed tomography. Scr Mater 59:1043–1046. https://doi.org/10.1016/j.scriptamat.2008.07.034
27. Penumadu D, Kim F, Bunn J (2016) Damage of composite materials subjected to projectile penetration using high resolution X-ray micro computed tomography. Exp Mech 56:607–616. https://doi.org/10.1007/s11340-015-0085-2
28. Maire E, Zhou S, Adrien J, Dimichiel M (2011) Damage quantification in aluminium alloys using in situ tensile tests in X-ray tomography. Eng Fract Mech 78:2679–2690. https://doi.org/10.1016/j.engfracmech.2011.07.004
29. Sham TK, Rivers ML (2002) A brief overview of synchrotron radiation. Rev Mineral Geochem 49:117–147. https://doi.org/10.2138/gsrmg.49.1.11
30. Burnett TL, McDonald SA, Gholinia A, Geurts R, Janus M, Slater T, Haigh SJ, Ornek C, Almuaili F, Engelberg DL, Thompson GE, Withers PJ (2014) Correlative tomography. Sci Rep 4:4711. https://doi.org/10.1038/srep04711
31. Maire E, Withers PJ (2014) Quantitative X-ray tomography. Int Mater Rev 59:1–43. https://doi.org/10.1179/1743280413Y.0000000023
32. Kim FH, Penumadu D, Patel P, Xiao X, Garboczi EJ, Moylan SP, Donmez MA (2016b) Synchrotron 4-dimensional imaging of two-phase flow through porous media. MRS Adv 1:2757–2761. https://doi.org/10.1557/adv.2016.505
33. Murakami Y, Beretta S (1999) Small defects and Inhomogeneities in fatigue strength: experiments, models and statistical implications. 2:123–147. https://doi.org/10.1023/a:1009976418553
34. Beretta S, Romano S (2017) A comparison of fatigue strength sensitivity to defects for materials manufactured by AM or traditional processes. Int J Fatigue 94:178–191. https://doi.org/10.1016/j.ijfatigue.2016.06.020
35. Edwards P, Ramulu M (2014) Fatigue performance evaluation of selective laser melted Ti–6Al–4V. Mater Sci Eng A 598:327–337. https://doi.org/10.1016/j.msea.2014.01.041
36. ASTM E8/E8M (2016) Standard test methods for tension testing of metallic materials. ASTM International
37. Kim FH, Moylan SP, Garboczi EJ (2019a) Preparation of cylindrical tensile specimens for simultaneous mechanical testing and X-ray computed tomography. NIST Interagency/Internal Report (NIST IR):8234. https://doi.org/10.6028/NIST.IR.8234
38. EOS GmbH - Electro Optical Systems (2009) EOS StainlessSteel GP1 for EOSINT M 270
39. Slotwinski JA, Garboczi EJ, Stutzman PE, Ferraris CF, Watson SS, Peltz MA (2014) Characterization of metal powders used for additive manufacturing. J Res Natl Inst Stand Technol 119:460–493. https://doi.org/10.6028/jres.119.018
40. Cheruvathur S, Lass EA, Campbell CE (2016) Additive manufacturing of 17-4 PH stainless steel: post-processing heat treatment to achieve uniform reproducible microstructure. JOM 68:930–942. https://doi.org/10.1007/s11837-015-1754-4
41. Jacob G (2018) Prediction of solidification phases in Cr-Ni stainless steel alloys manufactured by laser based powder bed fusion process. NIST Advanced Manufacturing Series (NIST AMS) 100-14. https://doi.org/10.6028/NIST.AMS.100-14
42. Luecke WE, Slotwinski JA (2014) Mechanical properties of austenitic stainless steel made by additive manufacturing. J Res Natl Inst Stand Technol 119:398–418. https://doi.org/10.6028/jres.119.015
43. Bonse U, Busch F (1996) X-ray computed microtomography (μCT) using synchrotron radiation (SR). Prog Biophys Mol Biol 65:133–169. https://doi.org/10.1016/S0079-6107(96)00011-9
44. Kardjilov N, Dawson M, Hilger A, Manke I, Strobl M, Penumadu D, Kim FH, Garcia-Moreno F, Banhart J (2011) A highly adaptive detector system for high resolution neutron imaging. Nucl Instrum Meth A 651:95–99. https://doi.org/10.1016/j.nima.2011.02.084
45. ASTM E1441 (2011) Standard guide for computed tomography (CT) Imaging
46. ASTM E1695 (2013) Standard test method for measurement of computed tomography (CT) system performance
47. Buzug TM (2008) Computed tomography from photon statistics to modern cone-beam CT. Springer-Verlag, Berlin
48. Tobin KW, Bingham PR, Gregor J (2009) Mathematics of neutron imaging. In: Bilheux HZ, McGreevy R, Anderson IS (eds) Neutron imaging and applications: a reference for the imaging community. Springer US, Boston, pp 109–127. https://doi.org/10.1007/978-0-387-78693-3_7
49. Nyquist H (1928) Certain Topics in Telegraph Transmission Theory. Trans Am Inst Electr Eng 47:617–644. https://doi.org/10.1109/T-AIEE.1928.5055024
50. Feldkamp LA, Davis LC, Kress JW (1984) Practical cone-beam algorithm. J Opt Soc Am A 1:612–619. https://doi.org/10.1364/JOSAA.1.000612
51. Kak AC, Slaney M (2001) Principles of computerized tomographic imaging. Society of Industrial and Applied Mathematics, New York
52. Buades A, Coll B, Morel J-M (2011) Non-local means Denoising image processing on line. 1:208–212. https://doi.org/10.5201/ipol.2011.bcm_nlm
53. Volume Graphics (2018) VG Studio Max 3.1. https://www.volumegraphics.com/
54. Bernsen J (1986) Dynamic thresholding of grey-level images. Paper presented at the international conference on pattern recognition, Paris, France
55. Phan TQ, Kim FH, Pagan DC (2018) Micromechanical response quantification using high-energy X-rays during phase transformations in additively manufactured 17-4 stainless steel, under review. Mater Sci Eng A

56. Garion C (2014) Mechanical properties for reliability analysis of structures in glassy carbon. World J Mech 4:79–89. https://doi.org/10.4236/wjm.2014.43009
57. Bohn RB, Garboczi EJ (2003) User manual for finite element and finite difference programs: a parallel version of NISTIR 6269 and NISTIR 6997. NIST Interagency/Internal Report (NISTIR) 6997
58. Garboczi EJ (1998) Finite element and finite difference programs for computing the linear electric and elastic properties of digital images of random materials. NIST Interagency/Internal Report (NISTIR) 6269
59. Henry BS, Luxmoore AR (1997) The stress triaxiality constraint and the Q-value as a ductile fracture parameter. Eng Fract Mech 57:375–390. https://doi.org/10.1016/S0013-7944(97)00031-3
60. Gurson AL (1977) Continuum Theory of Ductile Rupture by Void Nucleation and Growth: Part I—Yield Criteria and Flow Rules for Porous Ductile Media. J Eng Mater Technol 99:2–15. https://doi.org/10.1115/1.3443401
61. Needleman A, Tvergaard V (1984) An analysis of ductile rupture in notched bars. J Mech Phys Solids 32:461–490. https://doi.org/10.1016/0022-5096(84)90031-0